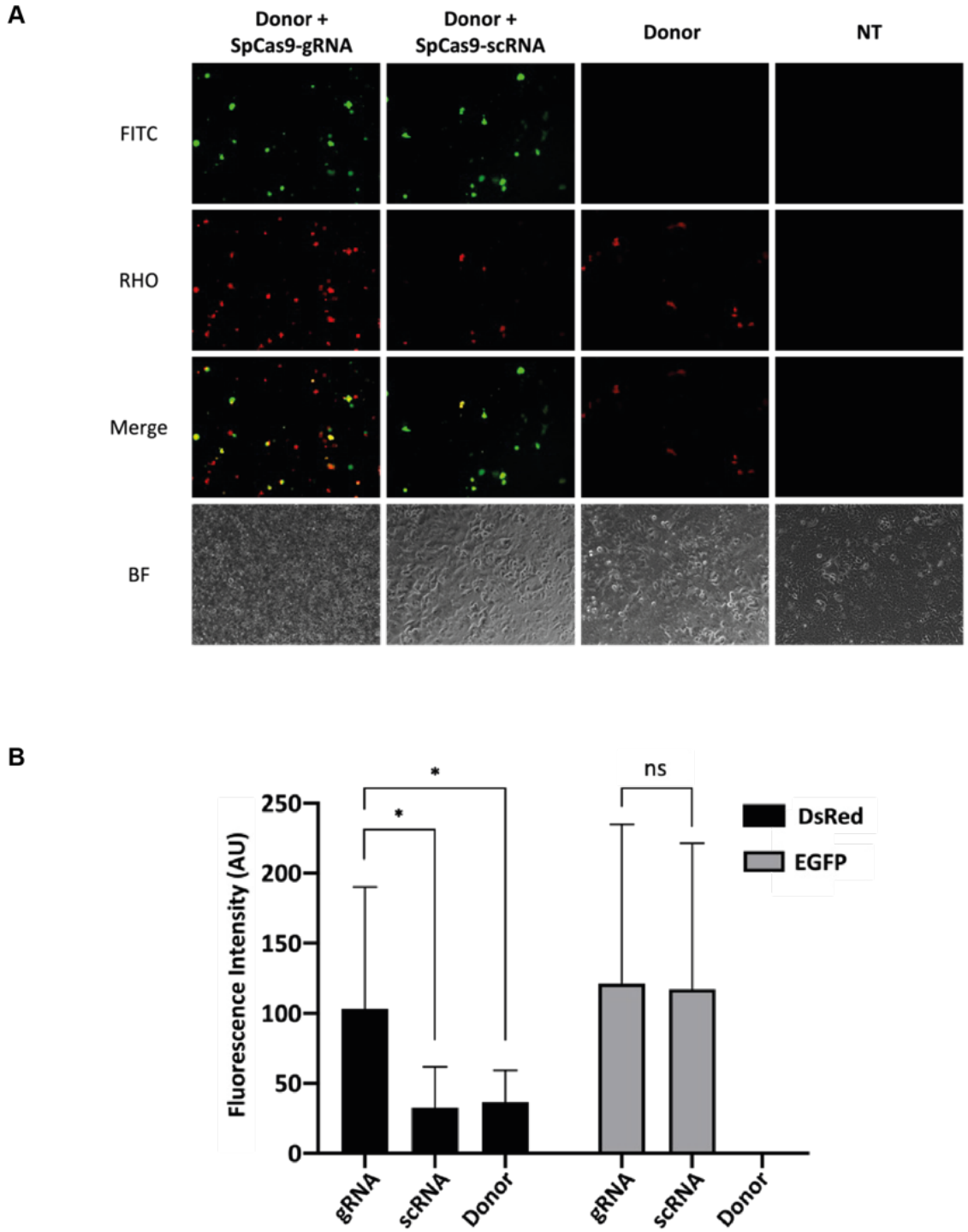


**Figure 24. In vitro validation of HITI-mediated integration into the 3' Alb locus. A)** Fluorescence microscopy imaging of transfected Hepa 1-6 cells with a mixture of SpCas9-gRNA (or -scRNA) and HITI donor or HITI donor alone. **B**) Quantification of the DsRed and EGFP fluorescence intensity of transfected cells, expressed in arbitrary units (AU). Significant differences between groups were assessed using one-way ANOVA with Tukey's post hoc test (*P<0.05, ns = not significant).

**AAV-HITI efficiency in neonatal mouse liver**

To investigate AAV-HITI efficiency in neonatal livers, I produced HITI vectors using the AAV serotype 8 which is known to have high liver tropism and has been safely and effectively used in various AAV-liver directed genome editing preclinical studies [95,115]. In this setting, one AAV delivers the large S. pyogenes Cas9 (SpCas9) under the expression of a small hybrid liver-specific promoter (HLP) to limit the nuclease expression only in targeted hepatocytes while the other AAV carries the HITI donor DNA, together with the promoter-less DsRed CDS and the U6 (gRNA or -scRNA) expression cassette. Newborn (post-natal day 1- or 2) wild-type mice were divided in two different group of treatment (AAV-HITI-gRNA or -scRNA) and then injected systemically via temporal vein, with a single AAV-HITI treatment at 1:1 ratio at a total dose of 1.2x10^14 genome copies (GC)/kg. One month post neonatal AAV-HITI delivery I harvested the livers of these mice, and I performed different histological and molecular analysis to assess HITI efficiency. By fluorescent microscopy images from liver cryo-sections, I found that Ds-Red was highly expressed in livers of mice treated with gRNA (mean ± SD =16±2.5% Ds-Red-positive hepatocytes; **Figure 25A**) but not with scRNA thus indicating productive HITI events. To further assess the total rate of HITI (including partial as well as reverse HITI events), I performed a customized DNA hybridization analysis with a probe specific for the HITI donor DNA vector on liver cryo-sections. By using this approach, I found about 40% more positive hepatocyte nuclei in gRNA- than scRNA-treated samples (**Figure 25B**). To determine whether the observed results were due to true integration events rather than the persistence of AAV-HITI donor DNA following newborn delivery, I performed RT-PCR on genomic DNA obtained from livers harvested at different timepoints after AAV-treatment. I observed a significant drop in the amount of episomal AAV genomes already after one month (**Figure 25C**). This is consistent with the expected AAV genome loss over time due to hepatocyte proliferation at that age.

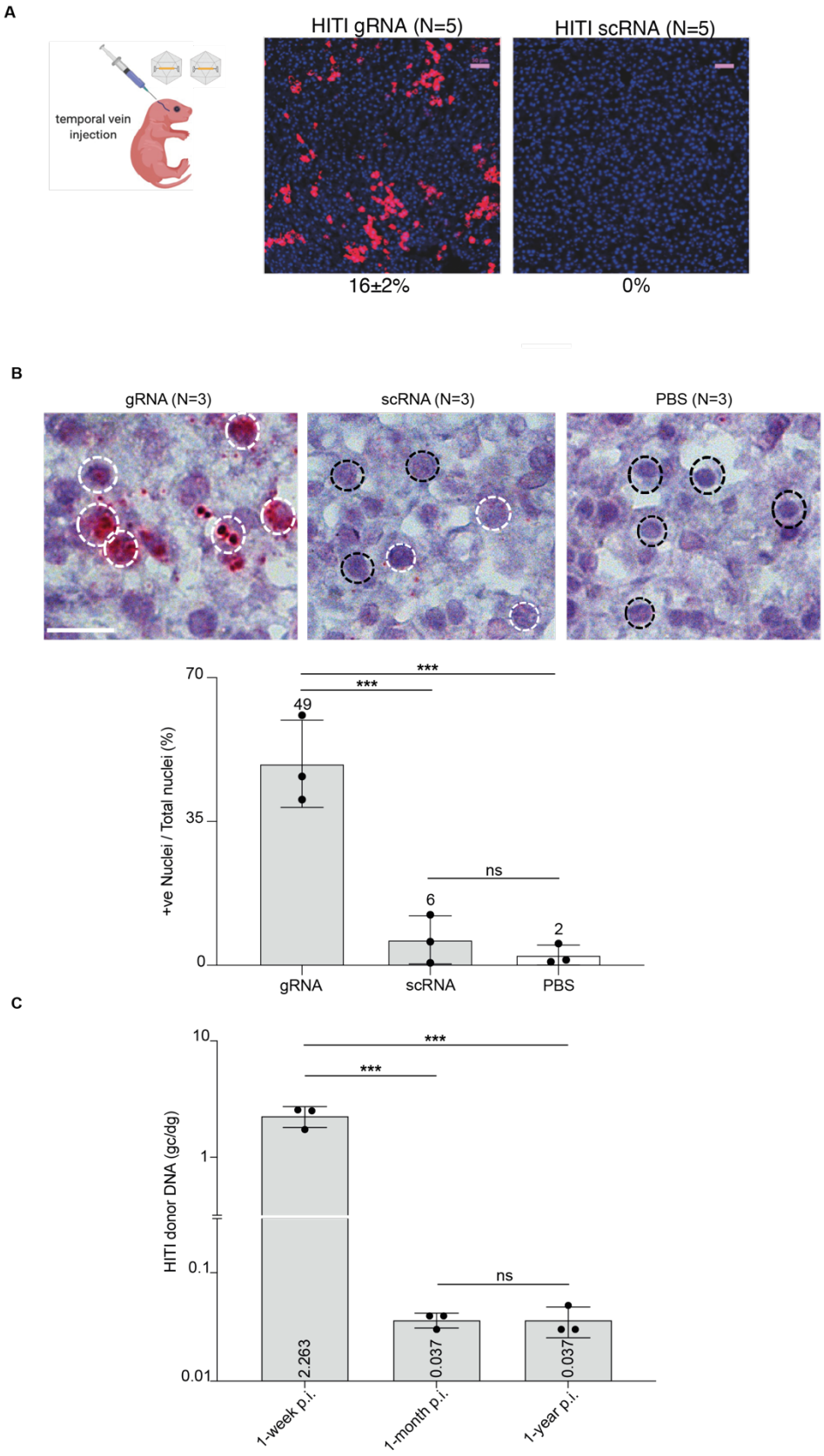


**Figure 25. AAV-HITI in newborn liver. A**) Representative fluorescence microscopy images of OCT liver cryo-sections from wild-type mice injected at post-natal day 2 with AAV-HITI

using the Ds-Red transgene (gRNA, N=5 or scRNA, N= 5) at the total dose of 1.2x10^14 total GC/kg. HITI efficiency is reported below the images. Scale bar 50μm. **B**) In situ Hybridization (ISH) of HITI donor DNA on liver sections. Upper panel: representative images of ISH in liver sections from (N=3) gRNA, (N=3) scRNA and (N=3) PBS experimental groups; Nuclei are stained in blue. White circles: positive nuclei; Black circles: negative nuclei; Scale bar of all images represent 25μm.Lower panel: quantification of positive nuclei over the total counted nuclei (+ve Nuclei/Total nuclei). Statistical differences were assessed by Ordinary one-way ANOVA Test followed by Tukey's multiple comparisons test. P-value*** = 0.0008 between gRNA and scRNA samples; p-value ***= 0.0005 between gRNA and PBS samples. Data are represented as mean ± standard deviation. **C**) Real-Time PCR analysis of HITI Donor vector genome in liver of AAV-HITIgRNA-treated newborn mice at different timepoints. Data are represented as mean ± standard deviation of HITI donor DNA genome copies/diploid genomes (gc/dg). For each timepoint N=3 samples were analyzed. Statistical differences were assessed by Ordinary one-way ANOVA Test followed by Tukey's multiple comparisons test. P-value***= 0.0001 between 1-week and 1-month; p-value ***= 0.0001 between 1-week and 1-year; p-value >0.999 between 1-month and 1-year.

## The role of the AAV-ITRs in mediating donor DNA integration

I then investigated whether the AAV-HITI donor DNA was integrated before or after being processed by CRISPR/Cas9 (therefore with or without the ITRs, respectively). For this purpose, I generated a control donor DNA vector lacking the inverted gRNA sites at both its 5' and 3' extremities (donor DNA without gRNA target sites), which should be integrated exclusively with its ITRs. I randomly assigned wild-type newborn mice to two treatment groups, and I systemically injected via the temporal vein at post-natal days 1-2 with a total dose of 3.9x10^13 GC/kg. Both groups received the same AAV vector encoding for the nuclease (AAV-SpCas9), co-delivered with a second AAV carrying either the Ds-Red HITI donor DNA or the newly generated donor DNA without gRNA target sites. One-month post-treatment, I extracted genomic DNA from liver samples for molecular analysis. I PCR amplified the 5' junction using specific

primers (**Figure 26**) on DNA samples from all treated mice. A PCR product corresponding to the expected size (~260bp) of the ITR-mediated integration was observed in samples treated with the donor DNA without gRNA target sites, and the presence of ITRs was confirmed by Sanger sequencing. Two junction PCR products of different sizes (~260 and ~190bp; **Figure 26**) were found in the samples from the AAV-HITI group. Sanger sequencing analysis showed that the smaller and more abundant PCR product (~190bp) corresponded to the expected HITI-mediated integration while the higher (~260bp) and less represented PCR product to the result of ITR-mediated integration.

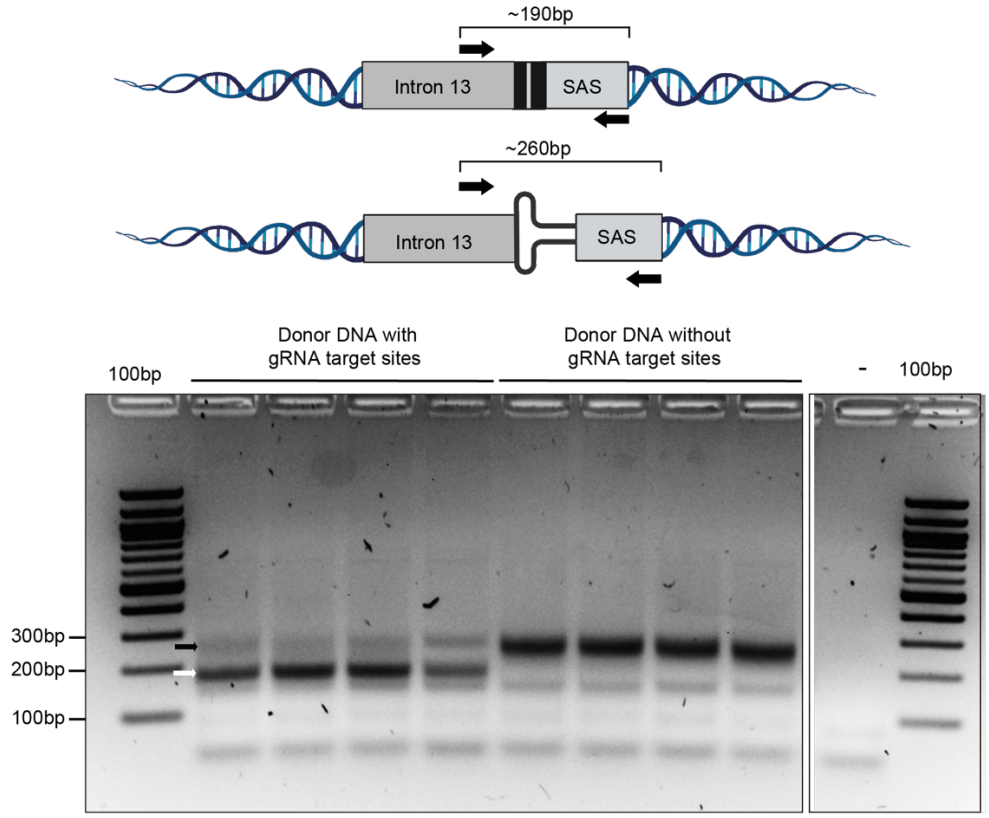


**Figure 26. Evaluation of HITI and AAV meditated integration at the albumin locus.** Schematic of the strategy with the expected PCR amplicons and the position of the primers (up), and representative images of the 5' junction PCR run on a 2% agarose gel (down). Four different biological samples for each group are showed in the gel. The white arrow indicates proper HITI-mediated donor DNA integration band (~190 bp); the black arrow indicates the ITR-mediated donor DNA integration band (~260 bp).

To further evaluate the role of the AAV- ITRs in mediating full-length donor DNA integration, I analyzed DNA samples from AAV-HITI-gRNA-treated mice by long-read (LR) sequencing using the Nanopore technology. To visualize the target-site after successful HITI, I PCR-amplified in separate reactions two different long PCR products (5' and 3'junctions; **Figure27A**) whose size corresponded to the full-length donor DNA integrated at the on-target (~2 kb; **Figure 27B**). In collaboration with the group of Prof. Toni Cathomen from Freiburg University, using a tailored bioinformatics pipeline, we count the reads that contained the ITR sequences. Importantly we found that only a minority 1.4% of all the 5' junction reads and 3% of all the 3' junction reads presented with remnants of ITRs.

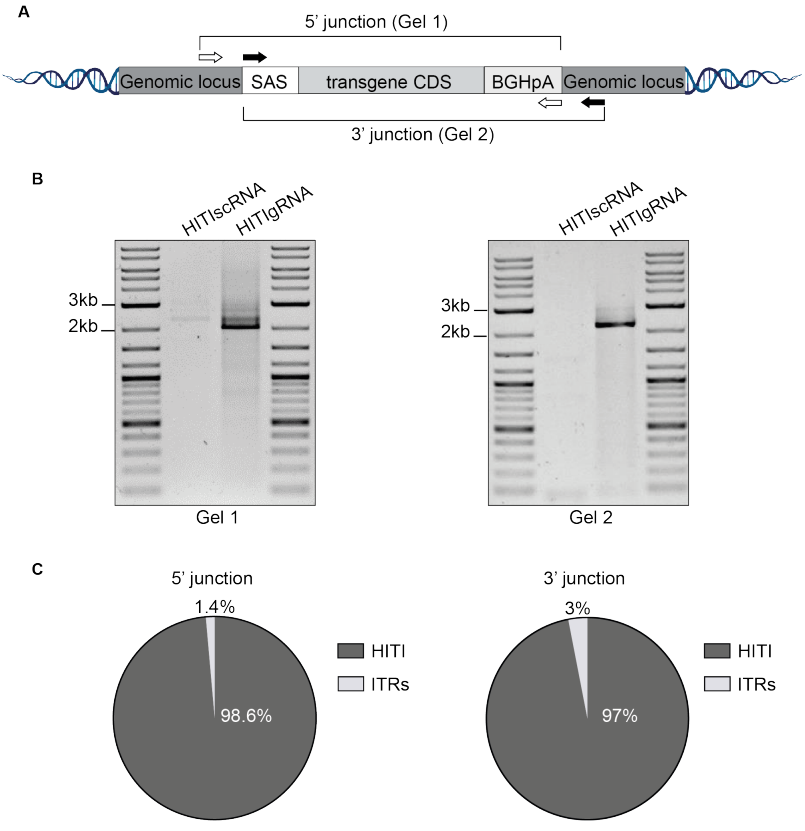


**Figure 27. Long reads analysis shows that full-length HITI donor DNA is integrated predominantly after ITR cleavage. A**) Schematic of the different long PCR junction products. White arrows indicate the primers designed to amplify the 5'junction: the forward primer (white left) was designed in the endogenous locus right before the cleavage site, the reverse

primer (white right) was designed at the end of the donor DNA on the polyadenylation signal (BGHpA). Black arrows indicate the primers designed to amplify the 3'junction: the forward primer (black left) was designed at the beginning of the donor DNA on the splicing acceptor signal (SAS); the reverse primer (black right) was designed in the endogenous locus right after the cleavage site. **B**) Representative images of the 5' and 3' junction PCR products run on an agarose gel for the detection of the full-length HITI donor DNA (~ 2 kb). The 5' junction is showed in Gel 1 and the 3' junction in Gel 2. **C**) Pie chart showing the percentage (%) of long reads in which donor DNA integration was HITI-mediated or ITRs-mediated (ITRs) at the junction sites.

## AAV-HITI molecular characterization

Next, to explore all the possible AAV-HITI outcomes at the on-target site, I performed comprehensive molecular analysis. I extracted genomic DNA from liver samples of AAV-HITI-treated mice. First, I assessed in vivo *Sp*Cas9-gRNA efficiency at the on-target site. For each treatment (gRNA or scRNA), I analyzed by targeted amplicon NGS a pool of 3 different DNA samples. Small insertions/deletions (indels) were observed in ~30% of reads from gRNA but not scRNA samples (~0.1%; **Figure 28**).

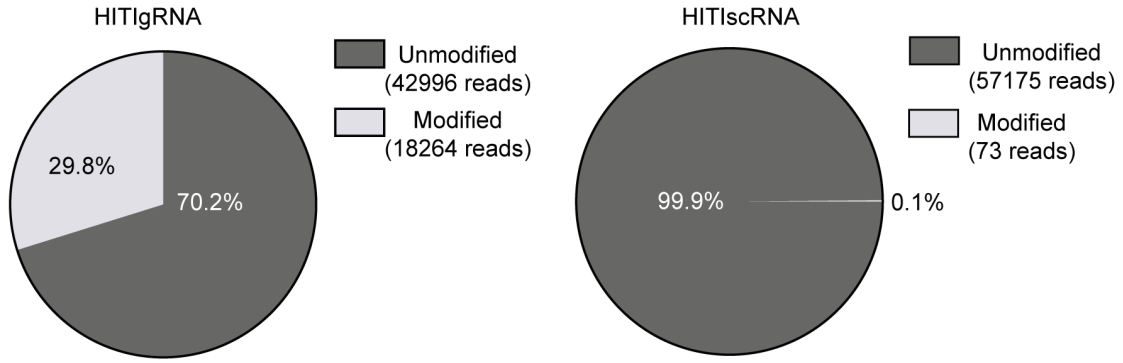


**Figure 28. Evaluation of gRNA efficiency in newborn mice treated with AAV-HITI**. Pie chart showing the modified reads observed in AAV-HITI (HITIgRNA or HITIscRNA) -treated mice analysed by next generation sequencing (NGS). The expected amplicon size is 285bp,

which was covered by 2x250bp reads in NGS. The percentage of the modified reads is used as an indication of the gRNA efficiency at the on-target site (HITIgRNA~30 % of indel).

Moreover, to assess the various donor DNA integration outcomes, I performed a customized CAST-Seq [129] analysis (**Figure 29**) in collaboration with the group of Toni Cathomen from Freiburg University.

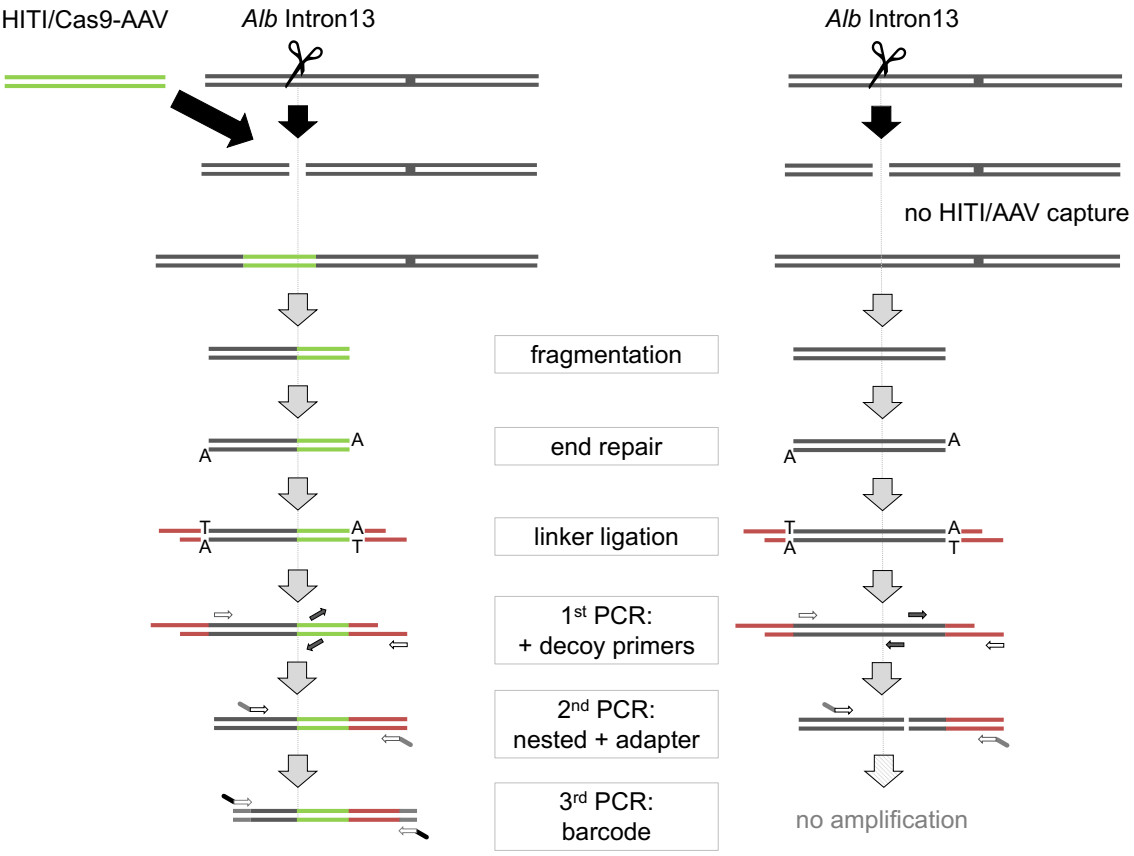


**Figure 29. Schematic representation of CAST-Seq at the on-target site.** The cartoon shows the CAST-Seq library preparation for e detection of integrated AAV-HITI vectors at the on-target site uponnuclease cleavage. Liver genomic DNA is fragmented randomly, and end repaired to add a 3′-A overhang which is used for ligation of a short linker (red). The first PCR is performed with bait and prey primers (white arrows) binding to the target site and the linker, along with decoy primers (black arrows) binding to the on-target locus near the cleavage site. The second PCR with nested primers adds adapters that are used in the third PCR to add barcodes.

CAST-Seq allowed the identification of six predominant integration events (**Figure 30A**): **i.** the correct HITI event in the desired orientation (peak 1); **ii**. a fusion of intron 13 with the polyadenylation signal (pA) -encoding region of the AAV vector (peak 2); **iii**. ITR-containing AAV fragments in both forward and reverse orientations (peaks 3 to 6; **Figure 30A-B**). Based on read coverage, we also estimated that the intended HITI fusion product accounts for about 20% of integration events. The most frequent integration events are capturing of ITR-containing AAV fragments, maybe because they are shorter than the transgene containing DNA sections (**Figure 30A-B**). Moreover, when we analyzed a sub-fraction of CAST-Seq reads, i.e. only reads representing integration of cleaved (ITR-free) HITI donor template (peak 1 and peak 2 of all integration events) we found that a total of 34.2% (i.e. 19.7% + 14.5%, peak 1 + peak 2 respectively) corresponded to ITR-free HITI donor integration events and 48% of these, are expected to be productive (**Figure 30C**). Of note, this 34.2% of ITR-free HITI events converge with the 49% HITI-positive nuclei observed in **Figure 25B.** Furthermore, the 48% of the total (34.2%) ITR-free HITI events (16.4%) aligns very well with the 16% Ds-Red-positive hepatocytes observed by fluorescence microscopy (**Figure 25A**).

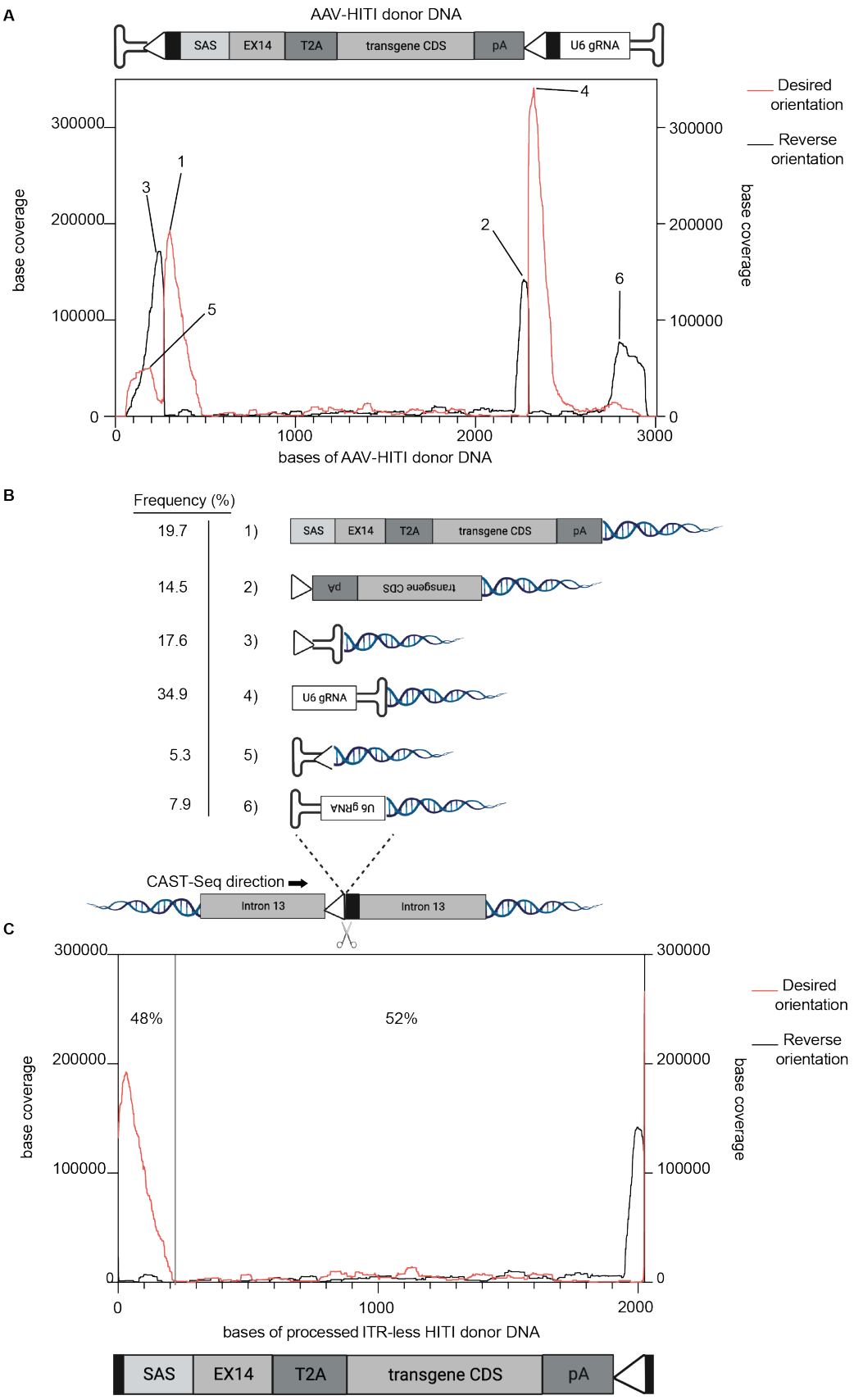
A
AAV-HITI donor DNA
SAS
EX14
T2A
transgene CDS
pA
U6 gRNA
Desired orientation
Reverse orientation
base coverage
bases of AAV-HITI donor DNA
B
Frequency (%)
19.7
14.5
17.6
34.9
5.3
7.9
CAST-Seq direction
Intron 13
C
48%
52%
bases of processed ITR-less HITI donor DNA

**Figure 30. Assessment of HITI integration events at the on-target site by CAST-Seq.**

**A**) Single base coverage of integration events by CAST-Seq. For each base, read coverage of the desired (forward strand) and reverse (reverse strand) integration is shown. Labelled are six distinct peaks that represent different integration events. **B**) Schematic representation of integration events. Shown are the six integration events corresponding to the peaks in (A), and their relative frequency determined by peak height. **C**) CAST-Seq based single base read coverage of cleaved transgene integration events. For each base, the read coverage of the desired integration and reverse integration is shown. The percentage of functional (left) versus non-productive integration (right) events are indicated.

## Evaluation of AAV-SpCas9 biodistribution, integration and expression in liver of newborn AAV-HITI treated

To evaluate potential SpCas9 related safety concern following neonatal treatment, I first monitored the amount of AAV-SpCas9 genomes over time in newborn mice and I found almost undetectable levels of AAV-nuclease genome already after one month (**Figure 31A**) consistent with data in **Figure 25C**. To further assess potential nuclease integration event at the on-target site, I employed CAST-Seq, and I found although at a lower frequency (peak at 60,000 reads, **Figure 31B**) compared to HITI donor DNA integration events (peak at 200,000 reads, **Figure 30A**) integration events of the nuclease within the on-target site. To qualitatively assess potential full-length AAV-*Sp*Cas9 integration events I performed long reads analysis. To this aim I designed specific primers as depicted (**Figure 31C**). A faint PCR fragment corresponding to the expected full length Sp.Cas9 size (~ 4.5kb) was amplified in the AAV-HITI gRNA- but not in the AAV-HITI scRNA-treated sample (**Figure 31C**). To understand whether this could result in *Sp*Cas9 expression I also performed Western blot analysis on AAV-HITI-treated liver lysates 1-year after vector delivery. No Cas9 expression was detected in the analyzed liver lysates (**Figure 31D**) suggesting that the risk of unwanted genetic editing due to long-term *Sp*Cas9 expression appears low under these conditions.

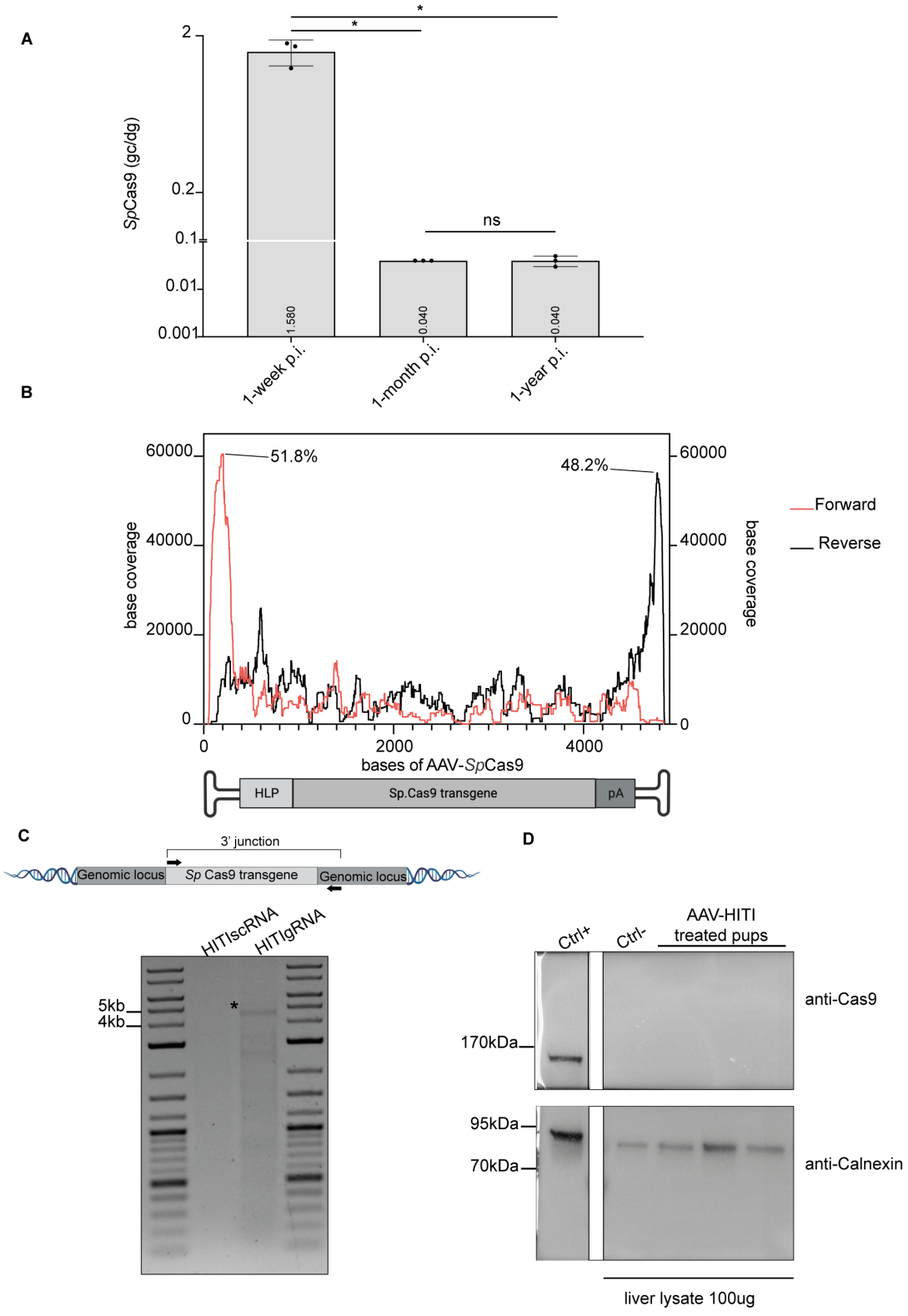


**Figure 31. Evaluation of AAV-SpCas9 biodistribution, integration and expression in liver of newborn AAV-HITI-treated mice.A**) Real-Time PCR analysis of Sp.Cas9 vector genome in liver of AAV-HITIgRNA-treated newborn mice at different timepoints. Data are represented as mean ± standard deviation of Cas9 genome copies/diploid genomes (gc/dg). At each

timepoint N=3 samples were used for the analysis. Statistical differences were assessed by Ordinary one-way ANOVA Test followed by Tukey's multiple comparisons test. P-value * = 0.0424 1-year. **B**) CAST-Seq based single base coverage of AAV-Sp.Cas9 integration events. For each base, the read coverage of the forward and reverse strand is shown. The relative frequency of capturing of the 5' and 3' ITR regions as determined by peak height is indicated. **C**) Schematic of the PCR analysis to detect full-length SpCas9 vector genome integration. Black arrows indicate the primers designed to amplify the 3'junction in the forward orientation: the forward primer was designed to bind in the HA-tag preceding the SpCas9 transgene; the reverse primer binds in the endogenous locus. The expected product size is ~ 4.5kb. **D**) Western blot analysis performed on liver lysates (100µg) extracted from AAV-HITI-treated mice 1-year after neonatal administration (AFgRNA N=3). Positive control (Ctrl+): cell lysate transiently transfected with a plasmid carrying the SpCas9. Negative control (Ctrl-): liver lysed obtained from a mouse left untreated.

## Assessment of CRISPR/Cas9-induced off-target effects in AAV-HITI-treated liver tissue

To evaluate potential CRISPR/Cas9-induced chromosomal rearrangements in an unbiased manner, I performed in collaboration with the group of Prof. Toni Cathomen a CAST-Seq analysis. This technology (originally developed to enable assessment of DNA aberrations between the on target and a putative off-target site) allows the detection of large deletions and inversions at the on-target site. CAST-Seq performed on genomic DNA extracted from liver samples of three different mice treated with AAV-HITI (gRNA or scRNA) resulted in no detectable translocation events (**Figure 32A**). Moreover, I also used an in silico prediction softwere (CRISPOR) to identify putative off-targets and I selected the top 10 candidates for downstream analysis (**Table 1**).

| gRNA specificity | Region | Position | (5'-3') gRNA + PAM sequences | Mismatches | Off-target CDF score |
|---|---|---|---|---|---|
| ON- target | Intron: albumin | chr5: 90622727-90622747:- | GTATTTAATAGGCAGCAGTG TGG | - | - |
| 1-OFF-target | Intron: Rik | chr5: 151333345-151333367:- | **T**TA**C**TTAATA**A**GCAGCAGTG TGG<br>* * * | 3 | 0.647 |
| 2-OFF-target | Intron: Lrr 1 | chr12: 69224137-69224159:- | GT**T**TTTAA**A**A**A**GCAG**A**AGTG GGG<br>* * * * | 4 | 0.646 |
| 3-OFF-target | Intergenic: Ppp1r3c-Tnks2 | chr19: 36774036-36774058:- | **T**TAT**C**TAATAG**A**CAGCA**A**TG CGG<br>* * * * | 4 | 0.646 |
| 4-OFF-target | Intron: Zim2 | chr7: 6660686-6660708:+ | G**A**ATTT**G**ATAG**A**CAGCAGTG GGG<br>* * * | 3 | 0.557 |
| 5-OFF-target | Intron:Slc39a12 | chr2: 14426612-14426634:+ | GTATTTA**GA**AGGCAGCAGT**T** TGG<br>** * | 3 | 0.476 |
| 6-OFF-target | Intron: Gstcd | chr3: 132751735-132751757:- | **AA**ATTT**G**AT**T**GGCAGCAGTG TGG<br>** * * | 4 | 0.474 |
| 7-OFF-target | Intron: Kcnc1 | chr7: 46060812-46060834:- | GTATTTAA**A**AGGC**T**G**A**AGT**A** AGG<br>* * * * | 4 | 0.464 |
| 8-OFF-target | Intergenic: Rik/Lhfpl3-Lhfpl3 | chr5: 23268978-23269000:+ | **A**TATT**C**AA**GT**GGCAGCAGTG AGG<br>* * ** | 4 | 0.446 |
| 9-OFF-target | Intron: Dpyd | chr3: 119141669-119141691:+ | **A**TATTTAATAGGCA**A**CA**T**T**T** AGG<br>* * * * | 4 | 0.395 |
| 10-OFF-target | Intron: HCn2 | chr10: 79561901-79561923:+ | G**G**ATT**C**A**G**TAGGCAGCAGT**T** GGG<br>* * * * | 4 | 0.392 |

**Table 1. Top predicted off target site selected with the CRISPOR webtool.**

I designed primers specific for each locus and I PCR-amplified the region surrounding the expected off-target cleavage site. Following the amplification, I sent for next-generation sequencing analysis the resultant PCR fragments and I analysed them for the presence of insertion/deletions (indels) mutations. Off-target indels were found to be almost undetectable or present at similar frequency in AAV-HITI-gRNA and -scRNA-treated samples **(Figure 32B)**.

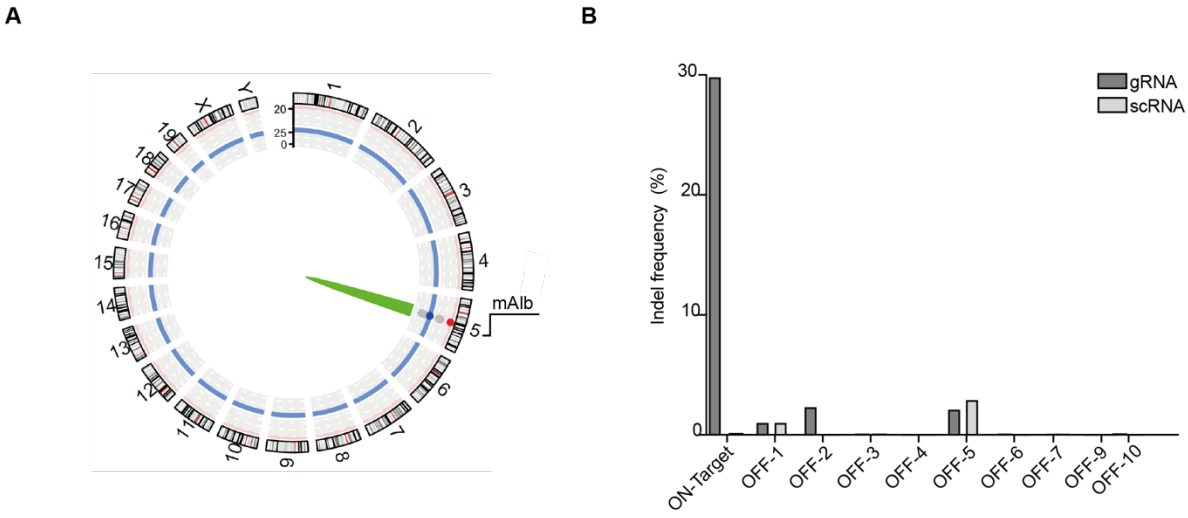


**Figure 32. Safety following neonatal delivery of high doses of AAV-HITI.A**) The circos plot summarize CAST-seq analysis performed on genomic DNA extracted from liver samples of AAV-HITI-treated MPS VI mice. The on-target is reported in green. No chromosomal aberrations were found. **B**) Off-target activity (indel frequency) measured at the top predicted off-target loci by next generation sequencing (NGS) analysis on genomic DNA extracted from liver samples of AAV-HITI-treated MPSVI. The off-target 8 (OFF-8) was excluded due to technical issues.

**Liver-directed AAV-HITI results in robust transgene expression following neonatal treatment in MPS VI and HemA mice**

After extensively characterizing the AAV-HITI platform at the molecular level, I explored its therapeutic potential in two different mouse models of human inherited diseases, targeting the liver for stable expression and subsequent secretion of therapeutic products into the bloodstream. For the first model, mucopolysaccharidosis type VI (MPS VI), a lysosomal storage disorder caused by Arylsulfatase B (ARSB) deficiency, I designed a HITI donor DNA carrying the ARSB coding sequence (CDS) in place of Ds-Red. AAV-HITI vectors were co-delivered systemically to newborn MPS VI mice at a 1:1 ratio, with a total dose of 1.2x10^14 genome copies (GC)/kg. Treated mice were monitored over a year, with monthly blood withdrawals to assess ARSB expression and secretion, as ARSB can be measured non-invasively in the bloodstream [21]. Starting from 1-month post-treatment, I found supraphysiological levels of the serum active ARSB in the sera obtained from AAV-HITI-gRNA-treated MPS VI (AFgRNA) mice compared to wild-type at all the analyzed timepoints, while AAV-HITI-scRNA-treated littermates (AFscRNA) had undetectable ARSB levels (**Figure 33A**).

For the second model, haemophilia A (HemA), the most common X-linked bleeding disorder caused by mutations in the *F8* gene, I designed a HITI donor DNA with a promoter-less CDS of a human B domain-deleted (BDD) *F8* variant (CodopV3 ~4.5 kb). Newborn HemA male mice were injected systemically with AAV-HITI vectors (gRNA or scRNA) at a total dose of 3.9x10^13 GC/kg. To evaluate AAV-HITI mediated efficacy in treated mice, I collected plasma samples at various timepoints, and measured F8 activity and antigen levels. In plasma samples obtained from AFgRNA-treated mice I found therapeutic levels of F8 up to 90 days post-treatment, with F8 protein levels around 40% of normal at 90 days post-treatment (**Figure 33B-C**).

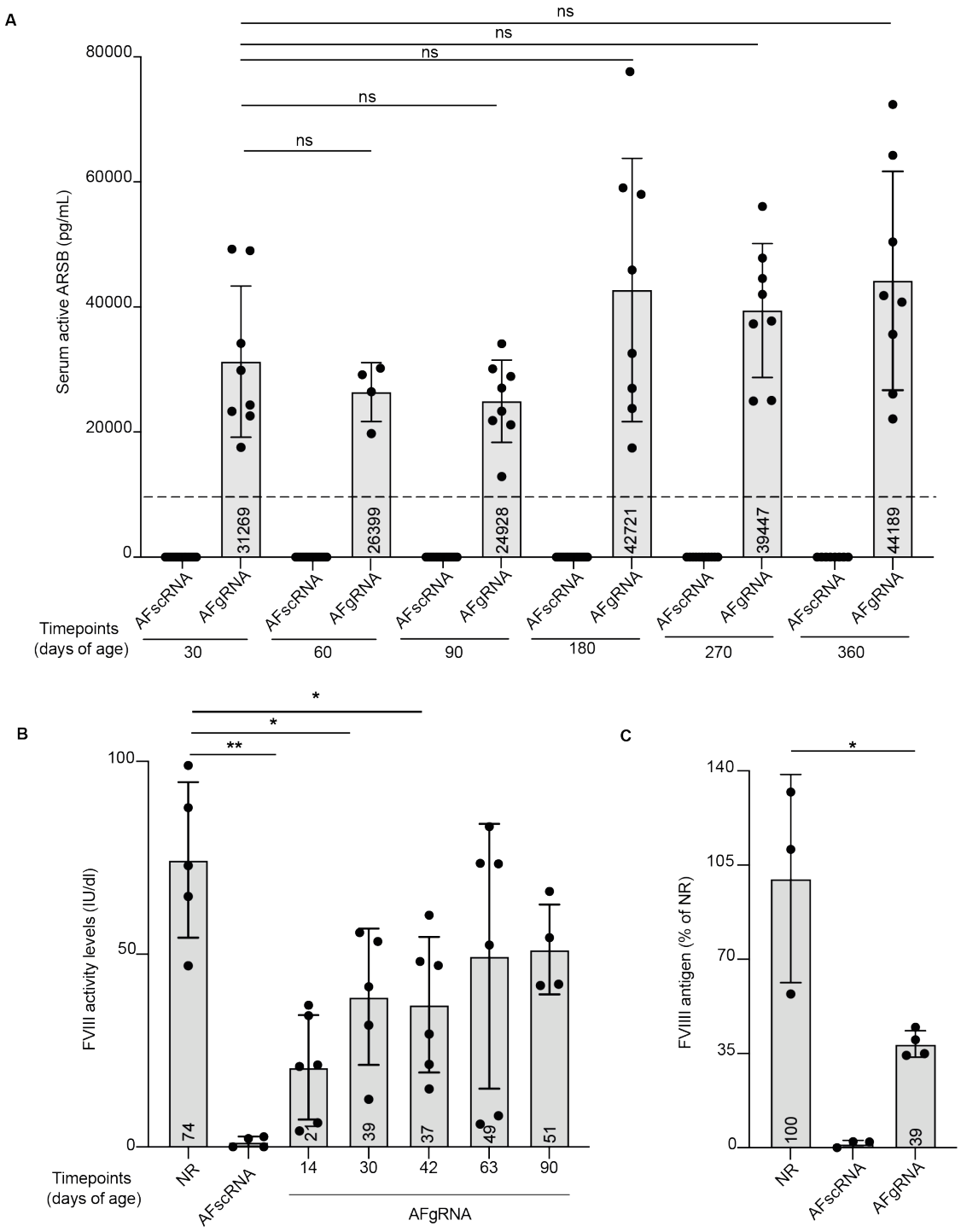


**Figure 33. AAV-HITI mediated transgene expression from newborn liver. A**) Serum ARSB activity was analyzed at different timepoints after AAV-HITI treatment. AFgRNA, MPS VI mice treated with AAV-HITI-gRNA (N= 8); AFscRNA (N=14 and N=8 survived up to p360), MPS VI mice treated with AAV-HITI-scRNA. Dotted line corresponds to normal serum ARSB

activity (NR= 11825±334 pg/mL; from Alliegro et al., 2016. [27]. ARSB measurements in all AFscRNA animals is equal to zero while all treated mice show ARSB activity levels higher than zero, therefore all the comparisons between the two groups are significant. No statistically significant differences were observed in AFgRNA-treated mice among the different timepoints. **A-C**) Each dot corresponds to a single animal within each group at different time points. **B**) F8 activity levels evaluated in Hema mice by chromogenic assay at different timepoints after AAV-HITI treatment. Statistical differences were assessed by ordinary one-way ANOVA test. P-value ** = 0.0025, between NR (N= 5) and AFgRNA (N=6) at 14 days; p-value * = 0.0190, between NR and AFgRNA (N=5, one sample was excluded) at 30 days; p-value *= 0.0389, between NR and AFgRNA (N= 6) at 42 days. No statistically significant differences were observed between NR and AFgRNA at the following timepoints. **C**) F8 antigen levels measured in AFgRNA (N=4) Hema mice at 90 days of age. P-value * = 0.0262 between NR and AFgRNA at 90 days. All data are represented as mean ± standard deviation.

## Albumin expression following AAV-HITI treatment

To evaluate if our AAV-HITI approach could impair endogenous albumin expression I measured serum albumin levels in AAV-HITI-treated (gRNA or scRNA) MPS VI mice and unaffected littermates at p360, and confirmed that our AAV-HITI approach does not alter endogenous albumin expression (**Figure 34 A**). Furthermore, I investigated whether following AAV-HITI serum albumin includes the T2A modification (Alb-2A) as predicted based on the AAV-donor DNA design. To this aim I performed Western blot analysis. AAV-HITI-treated sera or plasma samples obtained from both MPS VI or HemA collected at different timepoints after treatment were analyzed and the presence of Alb-2A of correct size was confirmed (**Figure 34 B-C**).

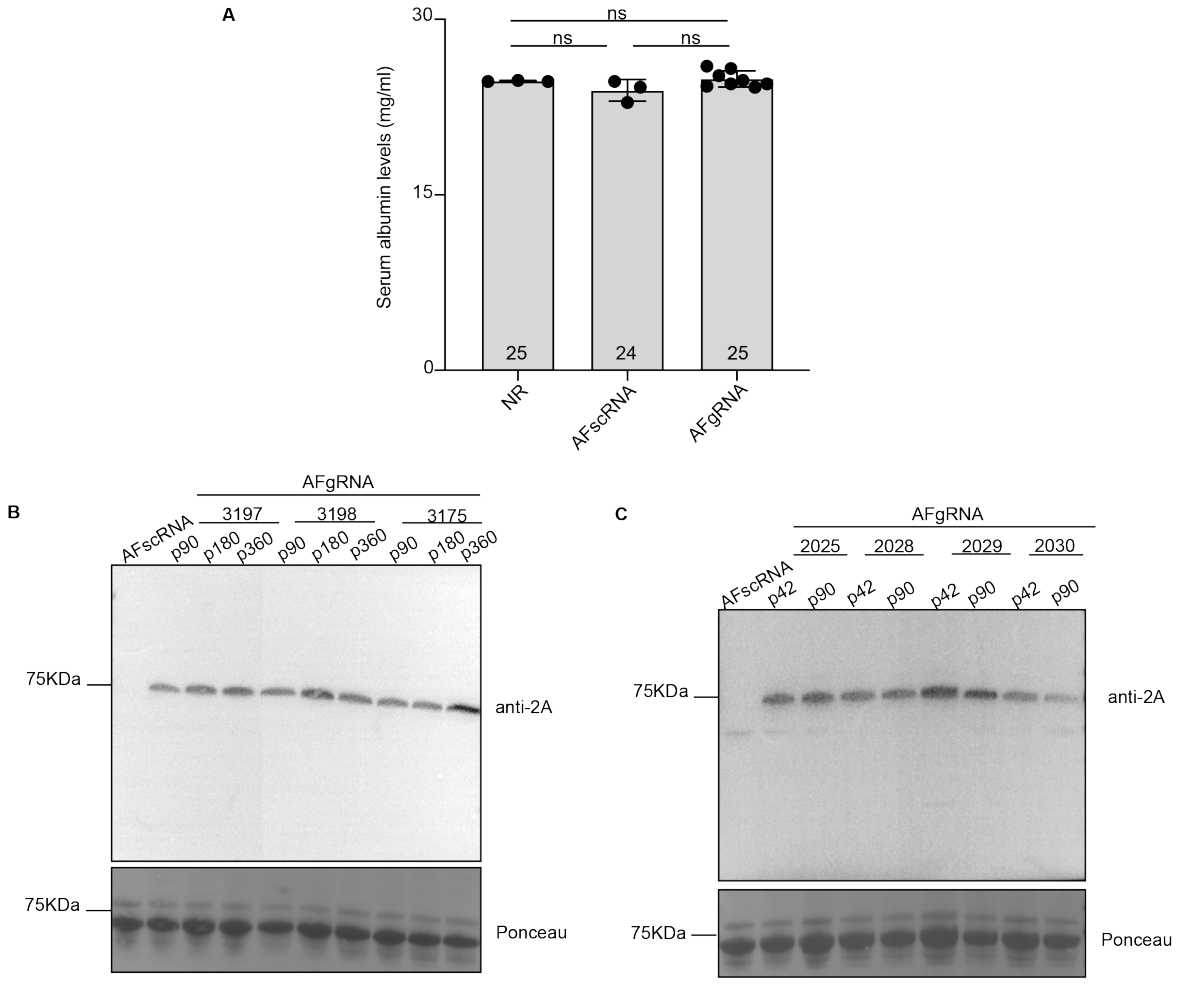


**Figure 34. Detection of the modified albumin 2A (Alb-2A) in sera from AAV-HITI treated mice.** **A**) Serum albumin levels measured 1-year post-treatment in sera samples from normal controls (NR, N=3) or AAV-HITI-treated MPSVI mice (AFgRNA, N=8; AFscRNA, N=3); data are represented as mean ± standard deviation. Statistical differences were assessed by ordinary one-way ANOVA test.**B**) Western blot analysis performed on 10 µg of proteins extracted from sera samples collected from AAV-HITI-treated MPS VI or HemA **(C)** mice to detect the modified Alb-2A (AFgRNA MPS VI N=3: 3197,3198,3175; AFgRNA HemA N=4: 2025,2028,2029,2030). In **A**) 3 different timepoints were analyzed: p90, p180 and p180 days post AAV-HITI neonatal delivery. In **C**) 2 different timepoints were analyzed: p42 and p90. An affected AAV-HITI scRNA-treated mouse (AFscRNA; MPS VI in A or HemA in **C**) was used as negative control.

**Liver-directed AAV-HITI improves the phenotype of MPS VI and HemA mice**

To evaluate AAV-HITI mediated phenotypic improvement, I then measured the GAG content in urine samples obtained from AAV-HITI treated and unaffected MPS VI mice at various timepoints. Three months post-treatment (p90) normalized urinary GAG levels in AFgRNA-treated MPS VI mice at similar to those in unaffected mice and remained stable up to the final analysis at one year (p360; **Figure 35A**). One year after treatment, I collected different organs for further analysis and found that GAG levels in liver, kidney, and spleen lysates of AFgRNA-treated MPS VI mice were normalized (**Figure 35B**). Correspondingly, GAG storage was significantly reduced in histological sections of these tissues, as well as in the heart mitral valve and myocardium (**Figure 35C**). This is particularly relevant because MPS VI patients often suffer from heart failure, mainly due to mitral valve insufficiency[152]. Additionally, I also investigated whether AAV-HITI could improve skeletal abnormalities, another feature of MPS VI. Radiographic images of the skull and long bones (femurs and tibias) were taken from AAV-HITI-treated MPS VI mice (AFgRNA or AFscRNA) and unaffected controls (NR), analyzing male and female mice separately due to sex-dependent growth differences. AFgRNA-treated mice showed an improved skull width/length ratio compared to AFscRNA-treated mice of the same sex (**Figure 35D**). I also noted lengths improvement in the femur (**Figure 35E**) and tibia (**Figure 35F**) of AFgRNA-treated male mice. In parallel I also investigated AAV-HITI therapeutic efficacy in newborn HemA mice (treated with either AFgRNA or AFscRNA). Specifically, I evaluated the hemostasis activity through tail-clip and activated partial thromboplastin time (aPTT) assays. I found that AFgRNA-treated HemA male mice exhibited a significant reduction of bleeding time (**Figure 35G**) and blood loss (**Figure 35H**) at 63 days of age and improved coagulation compared to AFscRNA-treated mice at 90 days of age (**Figure 35I**).

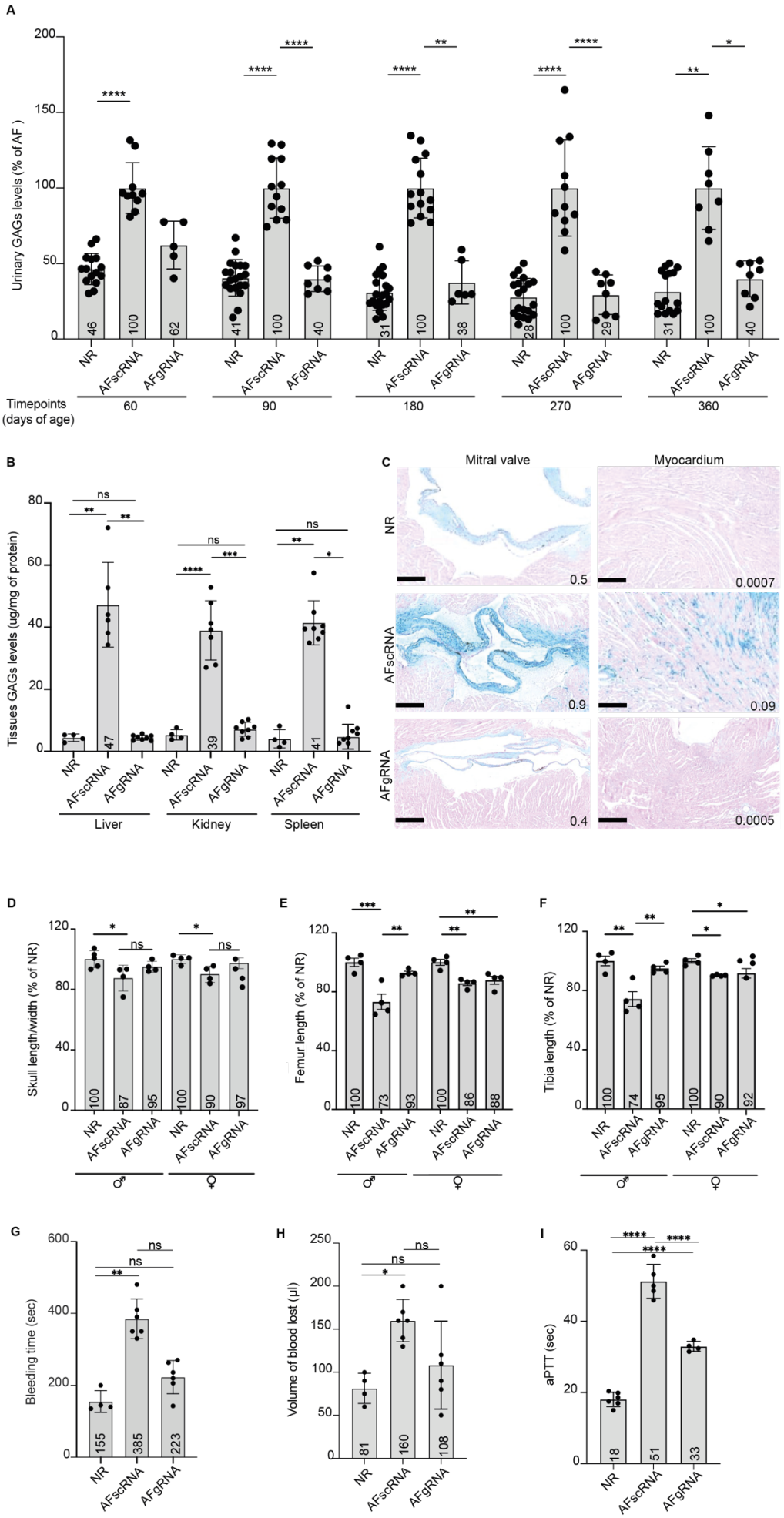
A
Urinary GAGs levels (% of AF )
Timepoints (days of age)
60
90
180
270
360
NR
AFscRNA
AFgRNA
B
Tissues GAGs levels (ug/mg of protein)
Liver
Kidney
Spleen
C
Mitral valve
Myocardium
NR
AFscRNA
AFgRNA
D
Skull length/width (% of NR)
E
Femur length (% of NR)
F
Tibia length (% of NR)
G
Bleeding time (sec)
H
Volume of blood lost (µl)
I
aPTT (sec)

**Figure 35. Liver-directed AAV-HITI therapeutic efficacy in newborn mice.** **A**) Urinary levels of glycosaminoglycans (GAGs) reported as a percentage of GAGs levels in affected MPS VI mice (% of AF). Statistical differences were assessed by Kruskal-Wallis Test and Dunn's multiple comparisons test. **B**) Quantification of GAGs in the liver, kidney, and spleen. Statistical differences were assessed by Brown-Forsythe and Welch ANOVA tests. **A-B**) Each dot corresponds to a single animal within each group at different time points. **C**) Representative histological images of GAGs storage in mitral heart valve and myocardium. Scale bar 100µm. Alcian Blue quantification is reported inside the images as Alcian blue positive area/total area. NR, N=4; AFscRNA, N=8; AFgRNA, N= 8. **D-E-F**) Measurement of skull length/width ratio, femur, and tibia lengths; data are reported as the percentage of normal length (% of NR). Males and females were kept separate in the analysis. **G-H**) Tail-clip assay performed at 63 days of age in Hema AAV-HITI-treated male mice (AFgRNA, N= 6; AFscRNA, N=6) and unaffected (NR; N= 4) controls. **I**) Activated partial thromboplastin time (aPTT) measured at 90 days of age in Hema AAV-HITI (AFgRNA, N= 4 and AFscRNA, N= 5) mice and unaffected (NR, N= 6) controls.

Lastly, Histopathological analysis performed on liver sections from all AAV-HITI-treated (AFgRNA or AFscRNA) mice and unaffected controls showed no evidence of HCC at this stage (p360; **Figure 36**). Collectively, these findings support the use of AAV-HITI for therapies directed to newborn liver.

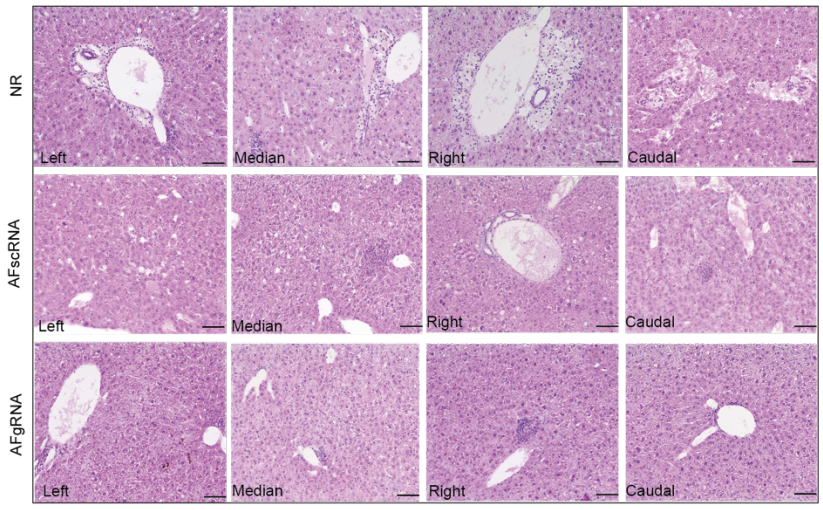

**Figure 36. Evaluation of hepatocellular carcinoma development in AAV-HITI-treated mice.** Representative images from histopathological analysis performed on paraffin sections from different liver lobes from AAV-HITI-treated MPSVI mice (AFgRNA, N= 8; AFscRNA, N= 8) and untreated normal controls (NR, N =4) 1-year post-treatment. Scale bar 50μm.

## Dose-response of liver-directed AAV-HITI in newborn mice

To determine the minimal AAV-HITI effective doses, I conducted a dose-response study in newborn MPS VI mice. I selected two additional doses of AAV-HITI that if directly translatable to humans, will be well tolerated: a medium dose (MD) of 3.9x10^13 total GC/kg and a low dose (LD) of 1.2x10^13 total GC/kg. To assess AAV-HITI efficiency at these new doses I used the AAV-HITI set of vectors where the HITI donor DNA contains the Ds-Red CDS. Newborn C57BL/6 mice were randomly assigned to the MD or LD group and injected systemically at p1-2, as described above. The percentage of hepatocytes expressing Ds-Red as a result of the integration (used to evaluated AAV-HITI efficiency) was quantified on liver cryo-sections 1-month post-treatment and found to be AAV dose-dependent (**Figure 37A**). Next, AAV-HITI efficacy at these same doses was evaluated in newborn MPS VI mice. I observed a similar dose-dependent effect on serum ARSB activity. Mice administered with AAV-HITI at MD, exhibited sustained and stable serum ARSB activity levels starting from 1-month post-treatment while mice treated with AVV-HITI at LD stably achieved ~50% of the normal ARSB levels (**Figure 37B**). Urinary (**Figure 37C**) and tissue GAG levels were normalized in AFgRNA-treated MPS VI mice (**Figure 38A-D**). GAGs storage was significantly decreased also in histological sections from the heart mitral valve and myocardium (**Figure 38E**) regardless of the dose used. Lastly, in MD AFgRNA-treated mice, I also observed a significant amelioration in the skull width/length ratio and in the femur length compared to AF controls (**Figure 38F-H**).

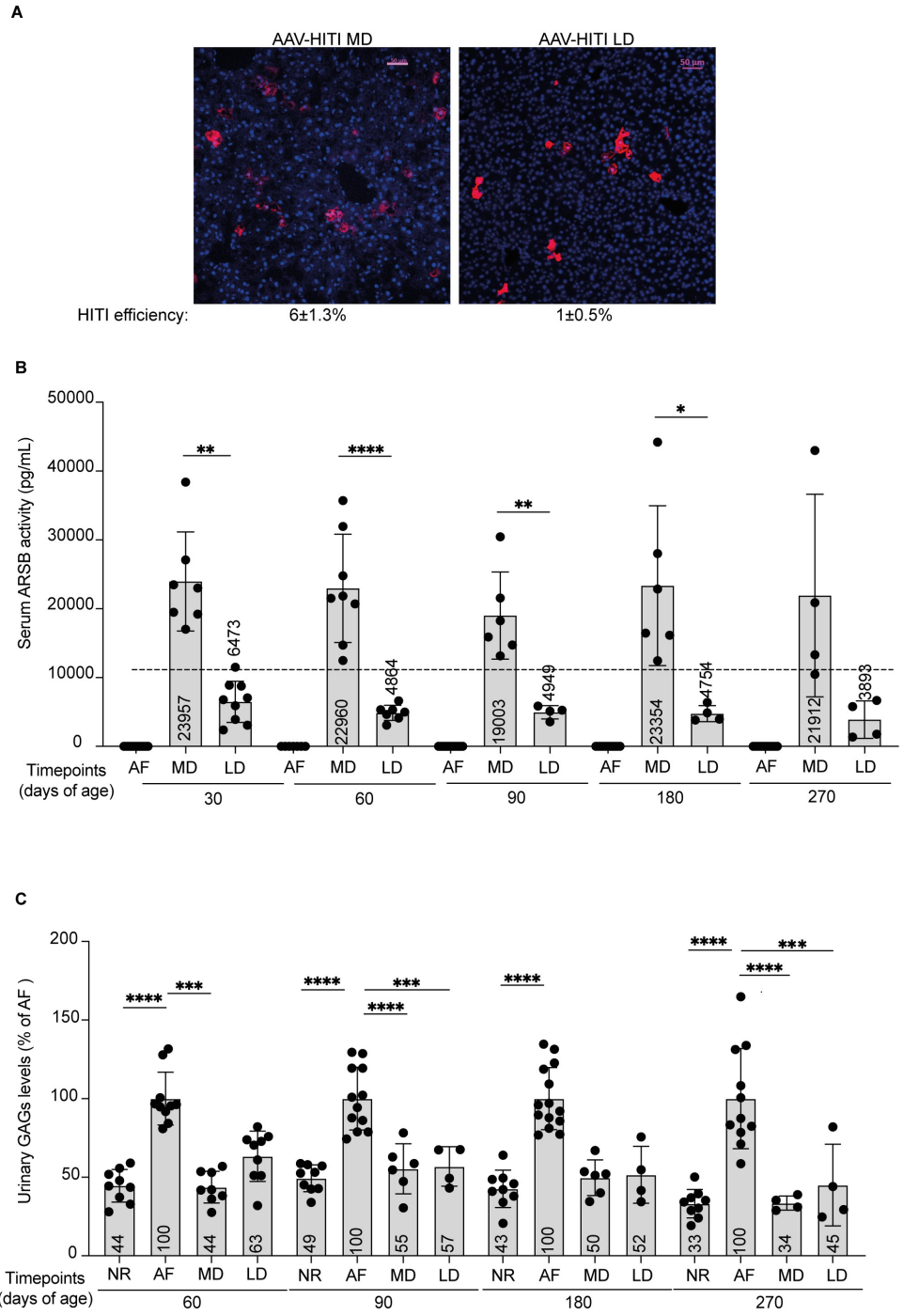


**Figure 37. Liver-directed AAV-HITI at various doses in newborn mice. A**) Representative fluorescence microscopy images of OCT liver cryo-sections from mice injected with AAV-HITI at different doses. Wild-type mice were treated with a medium dose (MD N=5, 3.9x10^13 total GC/kg) or a low dose (LD N=5, 1.2x10^13 total GC/kg) of AAV-HITIgRNA vectors. The percentage of Ds-Red positive hepatocytes (HITI efficiency) is reported. Scale bar 50µm. **B**) MPS VI mice were either left untreated (AF, N=14) or treated with a medium analysed at different timepoints after administration. Dotted line corresponds to normal serum ARSB activity (11825±334 pg/mL; Alliegro et al., 2016). Statistical differences were assessed by the

ordinary one-way ANOVA and Tukey's multiple comparisons test; at p30 p-value ** =0.001; at p60 p-value **** < 0.001; at p90 p-value ** = 0.0052; at p180 p-value * =0.0302. **C**) Urinary GAGs were measured at different timepoints in MPS VI mice treated with either a medium (MD, N=8) or low dose (LD, N=9), of AAV-HITI-gRNA as in (**A**), or left untreated (AF, N=14); NR, N=9, normal mice. Values are reported as a percentage of GAGs levels in untreated MPS VI mice (% of AF). Statistical differences were assessed by Kruskal-Wallis Test and Dunn's multiple comparisons test at p60 p-value **** = <0.0001 between NR and AF; p60 p value ***= 0.0026 between AF and MD. Statistical differences were assessed by Welch ANOVA Test and Dunnett's T3 multiple comparisons test at p90 p-value **** = <0.0001 between NR and AF; p90 p-value ****= 0.0033 between AF and MD; p90 p-value ***= 0.0082 between AF and LD. Statistical differences were assessed by Kruskal-Wallis Test and Dunn's multiple comparisons test at p180. P-value ****= 0.0005 between NR and AF; at p270 p-value ****= < 0.0001 between AF and MD; at p270 p-value ***= 0.001 between AF and LD. Each dot corresponds to a single animal within each group at different time points. **B**-**C**) The differences in the number of analyzed samples within the same group of treatment at different timepoints was due to sample availability. All Data are represented as mean ± standard deviation.